Chapter 9
FINITE ELEMENT ANALYSIS OF CHALK BEHAVIOR

MATERIAL NONLINEARITY AND THE INITIAL STRESS METHOD

The displacement finite element formulation is described in detail in several references (Zienkiewicz and Taylor, 2000; Hughes, 2000). The basics of the formulation are omitted here. A description of the initial stress method (Zienkiewicz et al., 1969) to account for material nonlinearity is given in the following paragraphs.

Using the displacement finite element method, a vector of incremental nodal displacements $\Delta\mathbf{u}$ is related to the vector of applied incremental nodal forces $\Delta\mathbf{F}$ by the global stiffness matrix $\mathbf{K}$ for the structure being analyzed:

$$\Delta\mathbf{F} = \mathbf{K}\Delta\mathbf{u} \tag{9.1}$$

For finite element analyses, the incremental nodal forces are generally known while the incremental nodal displacements are sought.

The global stiffness matrix is calculated using some stiffness tensor $\mathbf{D}$, usually the elastic $\mathbf{D}^e$ or tangent elastoplastic constitutive stiffness tensor $\mathbf{D}^{ep}$:

$$\mathbf{K} = \int_V \mathbf{B}^T \mathbf{D}\mathbf{B}\, dV \tag{9.2}$$

In equation (9.2), V is the element volume and $\mathbf{B}$ is the strain-displacement tensor, representing the derivatives of the element shape functions $\mathbf{N}$. The global stiffness matrix is the sum of all element stiffnesses in the finite element mesh.

The load-displacement curve is nonlinear for materials which exhibit material nonlinearity, such as geomaterials (Figure 9.1).Therefore, the displacements calculated using equation (9.1) generally correspond to stresses which are not in agreement with the constitutive behavior the material. The nodal displacements must be corrected such that the stresses correspond to the constitutive behavior of the material, and the applied external forces are in equilibrium with the stresses within each element. The initial stress method described here is one procedure used to accomplish this.

For the initial stress method, the strain increment vector $\Delta\boldsymbol{\varepsilon}$ at each Gauss point may be calculated using the strain-displacement matrix:

$$\Delta\boldsymbol{\varepsilon} = \mathbf{B}\Delta\mathbf{u} \tag{9.3}$$

A trial stress $\boldsymbol{\sigma}^{tr}$ may be calculated using the constitutive stiffness tensor **D** which was used to form the element stiffness matrix for the element of interest:

$$\boldsymbol{\sigma}^{tr} = \boldsymbol{\sigma}^{0} + \Delta\boldsymbol{\sigma}^{e} = \boldsymbol{\sigma}^{0} + \mathbf{D}\Delta\boldsymbol{\varepsilon} \tag{9.4}$$

The stress increment $\Delta\boldsymbol{\sigma}^{e}$ in equation (9.4) represents the elastic stress increment, which reflects the fact that the elastic stiffness tensor is usually the constitutive stiffness tensor **D** which is usually used to form the global stiffness matrix.

As stated above, the trial stress $\boldsymbol{\sigma}^{tr}$ generally is not in agreement with the applied strain increment and the constitutive behavior for geomaterials. A converged final stress $\boldsymbol{\sigma}^{f}$ must be calculated using the constitutive equations for the material and an appropriate integration algorithm. The stress correction $\Delta\boldsymbol{\sigma}$ between the trial and final stresses is converted into a nodal elemental force vector $\Delta\mathbf{F}^{el}$:

$$\Delta\boldsymbol{\sigma} = \boldsymbol{\sigma}^{tr} - \boldsymbol{\sigma}^{f} \tag{9.5}$$

$$\Delta\mathbf{F}^{el} = \int_{V} \mathbf{B}^{T} \Delta\boldsymbol{\sigma}\, dV \tag{9.6}$$

The nodal force vectors for all elements are summed into a global correction force vector $\Delta\mathbf{F}$ and then applied to the structure using equation (9.1) to bring the structure into global force equilibrium (Figure 9.1). If the yield function $f < 0$ for all Gauss points in the structure, any required stress correction is due to time-dependent behavior and only a single corrective iteration is needed to attain global force equilibrium; if the yield function $f = 0$ for any Gauss points in the structure, multiple corrective iterations using the initial stress method are usually required to achieve force equilibrium (Figure 9.1). The initial stress method illustrated in Figure 9.1 uses the Newton-Raphson method to achieve global equilibrium, in which the tangent global stiffness matrix is formed at each iteration to calculate the incremental displacements.

The finite element code used for the simulations was implemented on a MATLAB platform. The code uses 8-noded three-dimensional quadratic elements with a linear displacement function in each dimension. The shape functions for each element are evaluated at eight Gauss points (two in each dimension). Global equilibrium is attained using the Modified Newton-Raphson procedure, in which the initial global stiffness matrix is used for all global iterations within a given loading step.

FINITE ELEMENT AMALYSIS OF PORE FLUID EFFECTS ON CHALK BEHAVIOR

The constitutive equations developed in Chapters 5, 6, and 8 to describe the behavior of North Sea chalks and other soft rocks apply at a given point in a continuum. To use the constitutive equations in finite element analysis, the strains and stresses are calculated at selected points (*i.e.*, Gauss points) in each finite element. The displacements for each node of the finite element mesh are calculated assuming that the same material properties apply at all points in a given finite element. Since the water saturation is generally not uniform throughout the element, the average properties which correspond to the average water saturation in an element are used to calculate the average values for the material properties which apply to that element. This procedure is based on a concept called "equivalent uniform water saturation."

Use of the equivalent uniform water saturation is shown conceptually in Figure 9.2. The weighted relative strength distribution in the element is first calculated as a function of the water saturation distribution in the element. This relative strength corresponds to an equivalent uniform relative strength and equivalent uniform water saturation everywhere in the element. For all model parameters, it is assumed for calculation purposes that the equivalent uniform water saturation and equivalent uniform relative strength are present everywhere in the element. An example is given in the following paragraphs.

For a model parameter which varies as a function of water saturation, the appropriate value of the parameter may be calculated if the water saturation is known. As described in Chapter 8, it is assumed that the value of parameter x varies as a function of water saturation S_w as follows:

$$x = x_{\min} + (x_{\max} - x_{\min})(1 - S_w)^b \tag{9.7}$$

where $x_{\max}$ and $x_{\min}$ are the maximum and minimum values of parameter x, corresponding to fully oil-saturated and fully water saturated conditions, respectively, and b is a fitting parameter. If $x_{\max} = 2$, $x_{\min} = 1$, and $b = 20$, then $x = 1.12$ for a water saturation $S_w = 0.1$. This value of parameter x is obtained for any saturation conditions in which one-tenth of the pore space in a given finite element is occupied by water; this applies if one-tenth of the pore space is fully water-saturated and nine-tenths is fully oil-saturated, if all the pores are saturated with a fluid that contains 10% water plus 90% oil, or for any intermediate saturation condition.

FINITE ELEMENT SIMULATIONS

Three finite element simulations have been performed to demonstrate the ability of the constitutive model and finite element code to simulate the behavior of chalk at different scales. A description of the finite element simulations follows:

1) Laboratory scale simulations: These simulations examine the effects of one-dimensional waterflooding and uniaxial compaction of a chalk sample in a laboratory apparatus due to water injection and movement of the waterfront through an initially oil-saturated sample. It is assumed that the waterfront moves through the sample at a constant rate in a piston-like manner. The water saturation is assumed to be its maximum value in the volume of sample that the waterfront has passed, and to be its minimum value in the volume of sample that the waterfront has not reached. Several simulations are performed to illustrate the influence of stress states, waterflooding rates, and sample discretization on the simulated mechanical behavior of chalk. The cylindrical sample has dimensions of 2 inches in length and 2 inches in diameter (Figure 9.3). The first two simulations replicate "fast" waterflooding in which the entire waterflooding procedure takes 2 hours; these loading conditions are similar to those of Homand and Shao (2000). For all simulations, all elements have an initial porosity of 0.42; the equivalent void ratio is 0.72. The values used for the material properties are shown in Table 9.1. One simulation is performed under hydrostatic stress conditions ($\sigma_a = \sigma_r = 18$ MPa), while the other is performed under near-K_0 conditions ($\sigma_a = 22.7$ MPa, $\sigma_r = 14$ MPa). For both simulations, a quarter-section of the sample is analyzed with the finite element mesh discretized into 20 elements in the axial direction. 40 loading steps are applied for both simulations in the first set. The second two simulations replicate a "slow" waterflooding in which a 40-hour waterflood is performed between two 180-hour creep stages; these loading conditions are similar to those for the waterflooding tests detailed in Chapter 8. Both simulations are performed under near- K_0 conditions ($\sigma_a = 22.7$ MPa, $\sigma_r = 14$ MPa). A quarter-section of the sample is analyzed with different discretizations; for one simulation, the 20-element discretization in the axial direction is used, while a 1-element structure is used in the second simulation. For the 20-element structure, it is assumed that the water saturation increases at a constant rate in each successive element as the simulated waterfront passes;

when one element becomes fully water-saturated, the next element starts to become waterflooded. For the 1-element structure, it is assumed that the water saturation increases at a constant rate, uniformly throughout the single element. 200 loading steps are applied for both simulations in this second set. A comparison between the second two simulations will demonstrate the use of the averaging procedure and the "equivalent uniform water saturation" concept as described in the previous section.

2) Borehole scale simulations: These simulations examine the effects of waterflooding in the originally oil-saturated near-borehole region of an injection well. Again, it is assumed that the waterfront moves through the chalk at a constant rate in a piston-like manner. Three separate simulations are performed to investigate the relative effects of water weakening (or change in material behavior) and pore pressure increase which occur due to water injection. The first simulation assumes only water weakening occurs; the second simulation assumes only pore pressure increase occurs; and the third simulation assumes both processes occur simultaneously. For all simulations, a quarter section of the near-borehole region is analyzed (Figure 9.4). The borehole has a diameter of 0.8 m, and the full section is a square with 80 m-long sides. The finite element mesh is discretized to include 78 elements, with only one element in the z-direction. Deformation proceeds under plane strain conditions. The initial stress conditions are slightly overconsolidated and close to K_0 conditions. The initial vertical effective stress for all elements in the mesh is 30 MPa, while initial horizontal effective stress for all elements is 16 MPa. The initial porosity for all elements is 0.35; the equivalent void ratio is 0.54. The values used for the material properties are shown in Table 9.2. In each applicable case, water weakening and/or pore pressure increase extends to a distance of 11 m from the center of the borehole. The water saturation increases in the elements through which the waterfront passes. In water-weakened regions, full water saturation is assumed. The pore pressure increase dissipates with radial distance from the edge of the borehole. The maximum increase in pore pressure is 10 MPa, adjacent to the borehole; the pore pressure increases by 1 MPa at a radial distance of 11 m from the center of the borehole.
3) Field scale simulation: These simulations examine the effects of pore pressure drawdown and oil production in the Ekofisk field. Two different simulations are performed to examine the effects of water-weakening on reservoir compaction and subsidence. It is

assumed that the field chalk is initially oil-saturated, and that the initial fluid pressure in the reservoir is equal everywhere. In both simulations, effective stresses increase everywhere in the reservoir due to pore pressure drawdown. One simulation assumes no weakening occurs; the other assumes that oil saturation is decreased by 1 percent everywhere in the reservoir to account for historic oil production volume for the first 10 years of operations. In both cases, the field fluid pressure is decreased by 25 MPa in the Ekofisk and Tor Formations (but not in the tight zone), which is equal to the maximum historic drawdown. For all simulations, a quarter section of the near-borehole region is analyzed (Figure 9.5). The full section is a parallelpiped with dimensions of 13 km x 10 km in plan view, and 3.6 km deep. The finite element mesh is discretized to include 315 elements. Deformation proceeds assuming that reservoir pressure (*i.e.*, horizontal stresses) are unchanged at the periphery of the mesh. The initial stress conditions are slightly overconsolidated and close to K_0 conditions. In the overburden and underburden (layers 1-5 and 9), the initial vertical total stress gradient is 21 MPa/km. The fluid pressure increases nonlinearly such that the initial fluid pressure in the reservoir is 49 MPa. The lateral earth pressure coefficients in the overburden and underburden, and reservoir, are 0.8 and 0.3, respectively. All values are close to those recommended by Nagel (1998). The initial porosity for all elements is 0.35; the equivalent void ratio is 0.54. The overburden and underburden are assumed to be transversely isotropic and linear elastic with a greater stiffness in the *x*-*y* plane than in the vertical direction. The reservoir is assumed to be isotropic and to follow the chalk model formulated in this dissertation. The material stiffness in the reservoir assumed to equal half of the value obtained from the correlations, and the plastic compressibility is doubled; these changes are meant to account for reduced stiffness due to the presence of fractures. Similarly, the elastic moduli chosen are equal to one-half those recommended by Nagel (1998). The values used for the material properties are shown in Table 9.3.

RESULTS AND DISCUSSION

Laboratory-Scale Simulations

Results of the laboratory-scale simulations are presented in Figures 9.6 to 9.14 and are discussed below. The strain-time results show the evolution of average strain over small intervals within

the sample, and are presented as if each element was instrumented with an individual strain gauge. Also shown are the average axial strain over the entire length of the sample, which represents the displacement of the piston in a triaxial cell. The axial intervals for which results are presented are shown in Figure 9.6. Results for "fast" waterflooding simulations under hydrostatic conditions and near-K_0 conditions, respectively, are shown in Figures 9.7 and 9.8. Figure 9.7 shows the evolution of axial and radial strain with time in four elements (elements 3, 8, 13, and 18) within the FE mesh for near-K_0 conditions, while the equivalent figures for hydrostatic stress conditions are shown in Figure 9.8. Figures 9.9 and 9.10 show the distribution of pore space in the sample as loading progresses.

The results in Figures 9.7 and 9.8 agree qualitatively with the results of Schroeder et al. (1998) and Homand and Shao (2000). The results indicate that (1) axial strain occurs in discrete "jumps" as the waterflood passes and pore fluid composition changes; (2) the response of lateral strain gauges occurs over longer time periods than that of the axial strain gauges; (3) radial strains are of much greater magnitude, and axial strains are of lesser magnitude, under hydrostatic stress conditions than under near-K_0 stress conditions; (4) average axial strain progresses at a nearly-constant rate during "fast" waterflooding events.

The results of Figures 9.9 and 9.10 indicate that at any given time, the distribution of voids throughout the sample is bimodal. In oil-saturated regions of the sample, the void ratio is very close to its original value, while in water-saturated regions, the void ratio is significantly less. In each region, the void ratio is nearly uniform. These results indicate that pore collapse in the chalk occurs immediately upon passage of the waterfront. The transition zone between the more-porous (*i.e.*, oil-saturated) region and less-porous (*i.e.*, water-saturated) region moves in the direction water flow as time passes. Evolution of void ratio in single-phase saturated regions as time passes is attributed to creep.

For the creep and "slow" waterflooding test simulations, Figure 9.11 shows the evolution of axial and radial strain, and void ratio, with time for the structure discretized into 20 elements. Figure 9.12 shows the evolution of average axial and radial strain in the 1-element structure. It is seen in Figure 9.11 that strain occurs uniformly throughout the sample during the initial creep stage. However, strain becomes nonuniform during the waterflooding stage as described for the fast waterflooding simulations, and remains nonuniform during the final creep stage. The nonuniform strain signature is absent from the results for the 1-element structure shown in Figure

9.12, since only one element is present in the structure. The distribution of voids in the discretized sample is shown in Figure 9.13. The distribution is uniform during the initial creep stage; as for the "fast" waterflooding simulations, the void ratio distribution is nonuniform during the waterflooding stage. However, the bimodal distribution of voids throughout the sample is much less pronounced for the slow waterflooding simulations. A greater range of void ratios is observed at any given time in Figure 9.13 than in either of Figures 9.9 or 9.10. These effects may be attributed to time-dependent strains which occur at different rates at different regions in the waterflooded region. Although the greatest reduction in void space is due to the effects of waterflooding, post-waterflooding creep contributes to nonuniform distribution of void space in the fully water-saturated region. At any given time, the greatest accumulated strain and least void space are present in a region which was waterflooded earliest.

Figure 9.14 compares the average axial strain and radial strain signatures for the simulations of the slow waterflooding test using the 20-element discretized FE mesh and using a single element. The average strain histories are nearly identical at all times. It is concluded that the algorithm using the "equivalent uniform water saturation" concept is able to represent the same large-scale behavior for finite elements which are nonuniformly saturated with multiphase fluids as for an assemblage of many finite elements with the same saturation conditions. The algorithm gives good results even though the local behavior is quite different for chalk saturated with different pore fluids.

Borehole-Scale Simulations

Results of the borehole-scale simulations are presented in Figures 9.15 to 9.20 and are discussed below. The stress distributions at the end of the simulations are shown in Figures 9.15 to 9.17 for the case in which waterflooding causes material weakening only, for the case in which waterflooding causes pore pressure increase only, and for the case in which waterflooding causes both material weakening and pore pressure increase, respectively. It may be seen in Figures 9.15 to 9.17 that radial and vertical stresses are all reduced in the waterflooded region, while the stresses are not changed from their initial values in the oil-saturated region far from the borehole. For the case in which only material weakening occurs, the tangential stresses increase adjacent to the borehole, while the tangential stresses are reduced in the waterflooded region for the other two cases. The stress state is that of hydrostatic compression ($\sigma_1 > \sigma_2 = \sigma_3$) in the region far from

the borehole, while the stress state approaches that of hydrostatic extension ($\sigma_1 = \sigma_2 > \sigma_3$) in the near-borehole region, especially for the two cases which include pore pressure increase.

It is apparent from the results shown in Figures 9.15 to 9.17 that the stress distribution in the waterflooded region is quite different for the three cases simulated. The distribution of each stress component at the end of the simulation is shown as a function of the three waterflooding cases considered in Figures 9.18 to 9.20. It is seen in Figure 9.18 that the distribution of radial stress is very similar for the two cases which include a pore pressure increase, while the radial stress is quite different for the case which includes material weakening only. In Figure 9.19, it appears that the tangential stress distribution is slightly different for all three cases. Figure 9.20 shows that the distribution of vertical stress is very similar for the two cases which include material weakening, while the vertical stress distribution is quite different for the case which includes pore pressure increase only. For the case in which waterflooding causes material weakening and pore pressure increase, all three stress components are reduced to their least values for the three cases considered. It may be concluded that the pore pressure increase caused by waterflooding most strongly influences the radial stress, while the material weakening caused by waterflooding has its greatest influence on the vertical stress. While the radial and vertical stresses are directly influenced by the effects of waterflooding, the tangential stress is less directly dependent on these effects and more dependent on the relative magnitudes of the radial and vertical stresses.

Field-Scale Simulations

Results for the two field-scale simulations are shown in Figures 9.21 to 9.24. Figures 9.21 show the maximum compaction and subsidence profiles in the North-South and East-West direction for the case in which no water-weakening occurs. Figure 9.22 shows the compaction and subsidence histories at the center of the reservoir for the same simulation. Figures 9.23 and 9.24 are the corresponding figures for the water-weakening case.

It may be seen that for both cases, compaction is greatest at the reservoir center and is generally restricted to the reservoir area, while the area of subsidence extends beyond the reservoir limits. The compaction-to-subsidence (C/S) ratio for both cases is very close to the measured value of 1.2. In both cases, the C/S ratio is approximately constant throughout the depressurization phase. It is seen that the compaction and subsidence rates increase greatly when

depressurization exceeds 15 MPa, indicating that inelastic deformation becomes dominant as effective stress increases.

The compaction and subsidence values increase substantially for the case in which water-weakening occurs. Even a 1 percent change in water saturation has great effects on subsidence. It may then be expected that continued operation of the field will lead to continued subsidence due to water-weakening.

REFERENCES

Gutierrez, M.S., Pokharel, G., and Hickman, R.J. (2004). JCRCAP3D version 1.0: Development of a three-dimensional finite element program for wellbore stability analysis based on the JCR cap constitutive model. Project report to ConocoPhillips.

Homand, S., and Shao, J.F. (2000). Mechanical behavior of a porous chalk and effect of saturating fluid. Mechanics of Cohesive-Frictional Materials, 5, 583-606.

Hughes, T.J.R. (2000). The Finite Element Method: Linear Static and Dynamic Finite Element Analyses. Dover, Mineola, New York, 682 p.

Nagel, N.B. (1998). Ekofisk field overburden modeling. Proceedings of Eurock ’98, Trondheim, Norway, 177-186.

Zienkiewicz, O.C., Valliappan, S., and King, I.P. (1969). Elasto-plastic solutions of engineering problems: initial stress finite element approach. International Journal for Numerical Methods in Engineering, 1, 75-100.

Zienkiewicz, O.C., and Taylor, R.L. (2000). The Finite Element Method. Butterworth-Heinemann, Oxford, 700 p.

Table 9.1. Values for the model parameters for the laboratory-scale waterflooding simulations.

Model parameter	Oil	Water
Bulk modulus K (MPa)	1660	730
Poisson's ratio ν	0.24	0.24
Reference time-line anchor N	1.19	1.17
Compression coefficient λ	0.16	0.16
Cap aspect ratio M	1.06	0.92
Eccentricity parameter R	0.65	0.65
Attraction a (MPa)	4	2
Creep parameter ψ	0.0050	0.0085
Minimum volumetric age $t_{v,\min}$ (hours)	1	1
Pore fluid exponent b	25	

Table 9.2. Values for the model parameters for the borehole-scale waterflooding simulations.

Model parameter	Oil	Water
Bulk modulus K (MPa)	3200	1610
Poisson's ratio ν	0.24	0.24
Reference time-line anchor N	0.95	0.92
Compression coefficient λ	0.115	0.115
Cap aspect ratio M	1.40	1.21
Eccentricity parameter R	0.50	0.50
Attraction a (MPa)	4	2
Adjusted failure shear stress ratio $\overline{\eta}_f$	1.42	1.24
Tensile strength p_t (MPa)	1.2	0.6
Creep parameter ψ	0.0050	0.0085
Minimum volumetric age $t_{v,\min}$ (hours)	1	1
Pore fluid exponent b	25	

Table 9.3. Values for the model parameters for the field-scale simulations.

Model parameter	Shale	Chalk	
		Oil	Water
Bulk modulus K (MPa)	---	1600	800
Poisson's ratio ν	0.33	0.24	0.24
Reference time-line anchor N	---	1.29	1.26
Compression coefficient λ	---	0.23	0.23
Cap aspect ratio M	---	1.40	1.21
Eccentricity parameter R	---	0.50	0.50
Attraction a (MPa)	---	4	2
Adjusted failure shear stress ratio $\overline{\eta}_f$	---	1.42	1.24
Tensile strength p_t (MPa)	---	1.2	0.6
Creep parameter ψ	---	0.0050	0.0085
Minimum volumetric age $t_{v,\min}$ (hours)	---	1	1
Pore fluid exponent b	---	25	
Horizontal elastic modulus E_h (MPa)	1120	---	---
Vertical elastic modulus E_v (MPa)	840	---	---

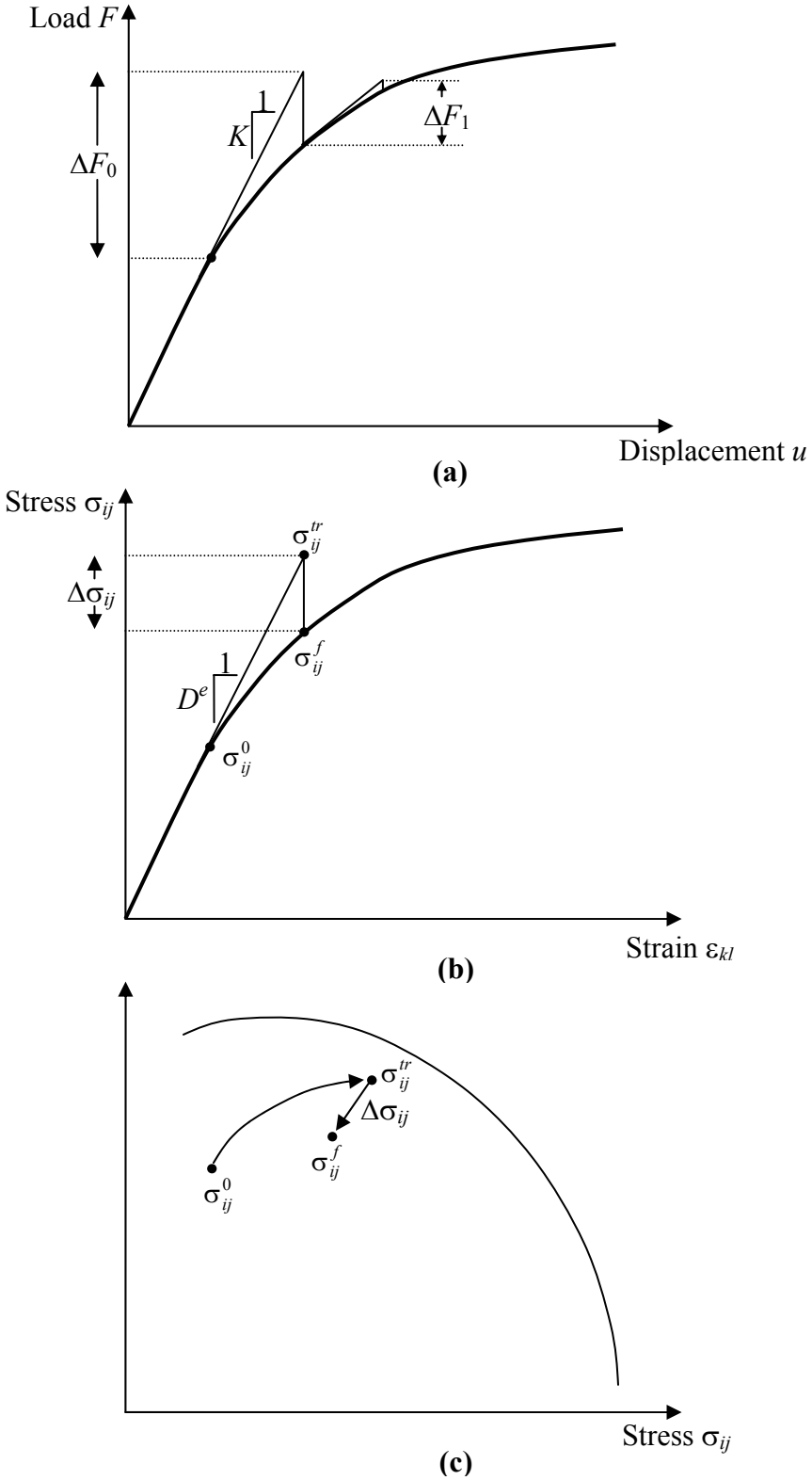

Figure 9.1. Schematic representation of initial stress method in finite element analysis of nonlinear materials in (a) load-displacement space; (b) stress-strain space; and (c) stress space. ΔF_0 is original applied load, ΔF_1 is correction load, $\Delta\sigma_{ij}$ is correction stress.

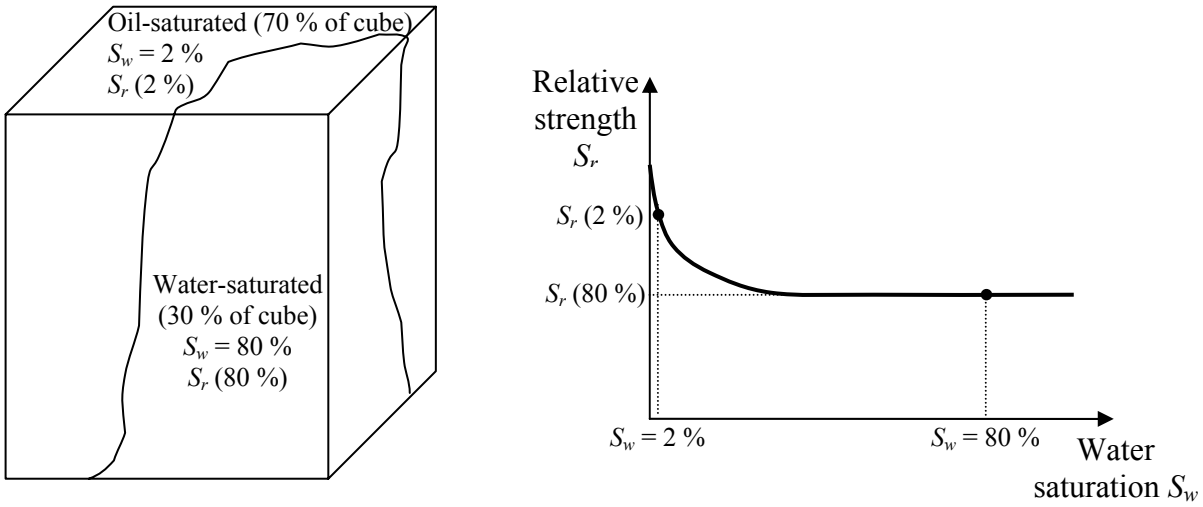

(a)

Equivalent uniform relative strength: $S_r = 0.7\ S_r\ (2\ \%) + 0.3\ S_r\ (80\ \%) = S_r\ (8\ \%)$
Equivalent uniform water saturation: S_w = 8 %

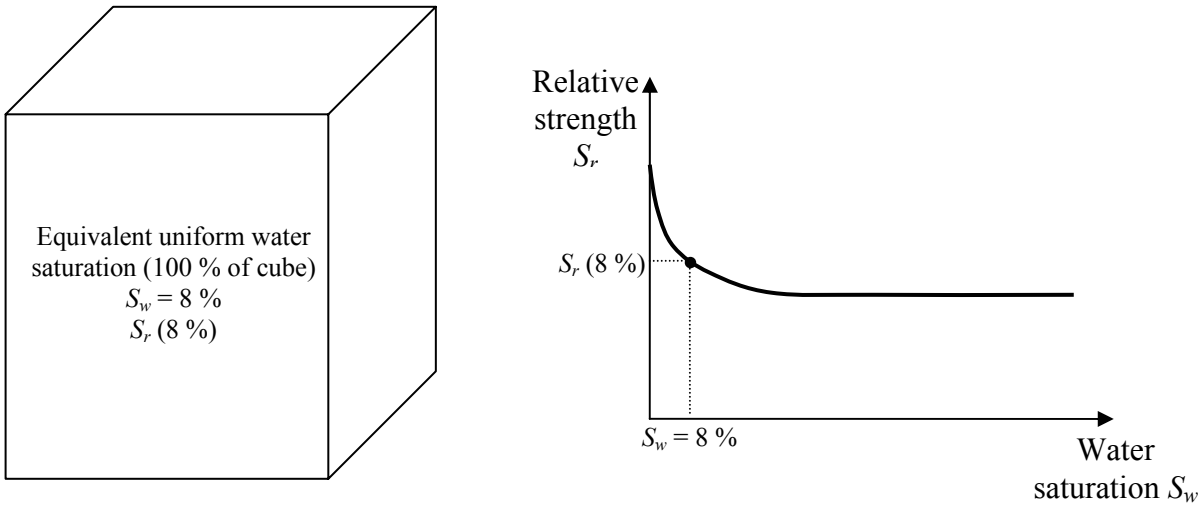

(b)

Figure 9.2. Schematic representation illustrating the concept of "equivalent uniform water saturation." Relative strengths and saturations for multiphase fluid saturated element are shown in (a); equivalent uniform relative strength and equivalent uniform water saturation is shown in (b).

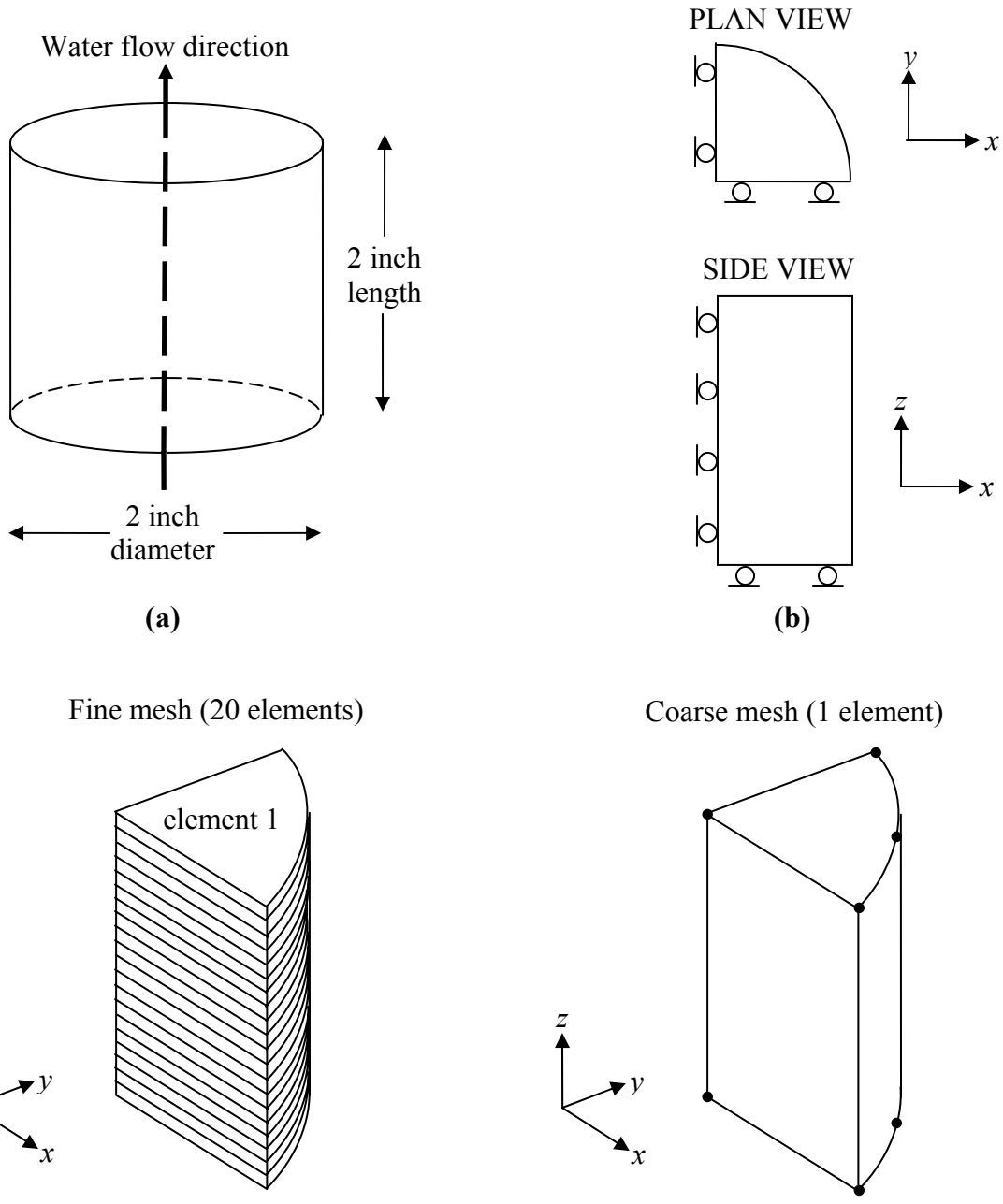

Figure 9.3. Geometry for laboratory-scale simulations. (a) Sample dimensions; (b) finite element boundary conditions; (c) finite element meshes used.

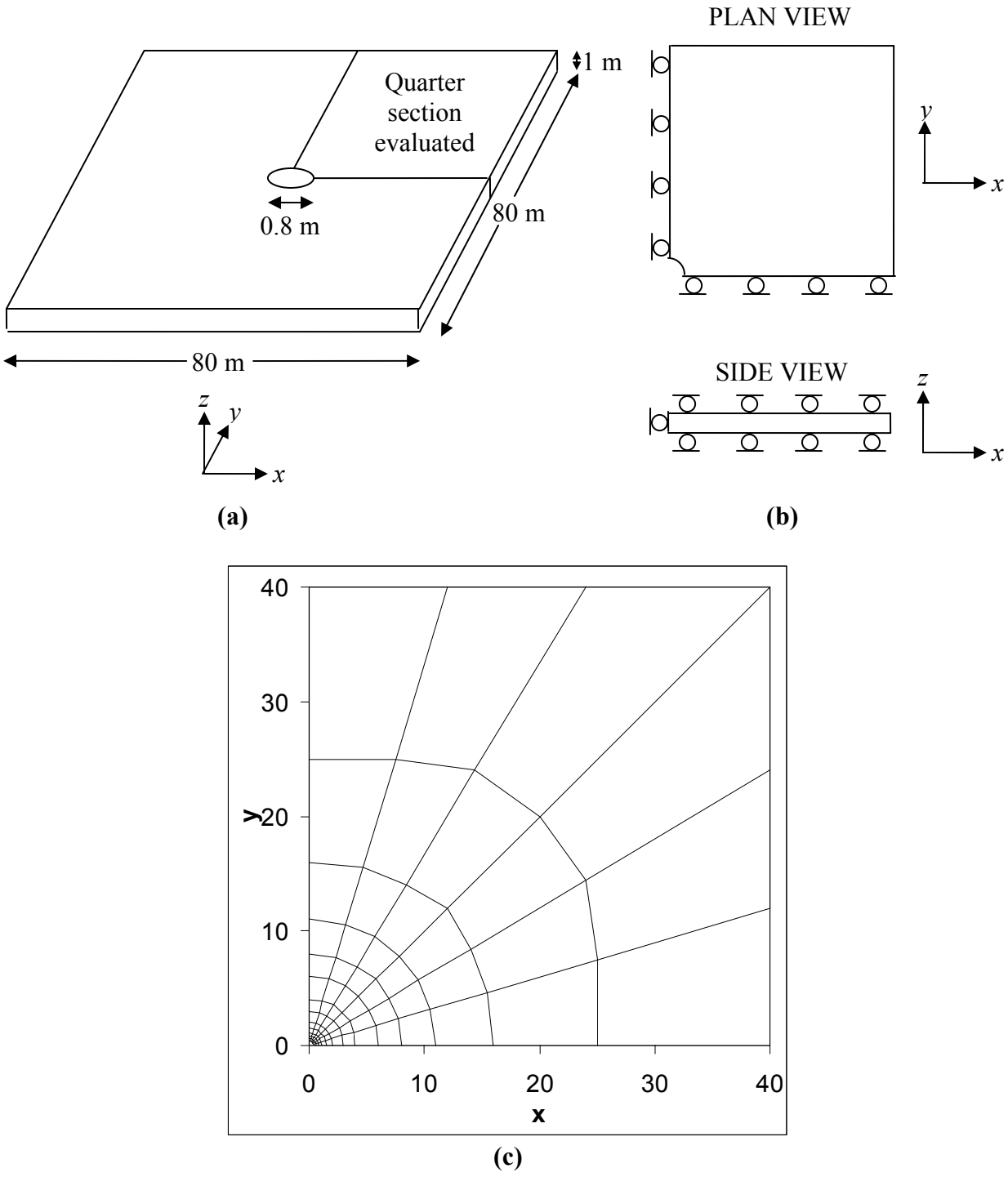

Figure 9.4. Geometry for borehole-scale simulations. (a) Dimensions of region evaluated; (b) finite element boundary conditions; (c) finite element mesh used.

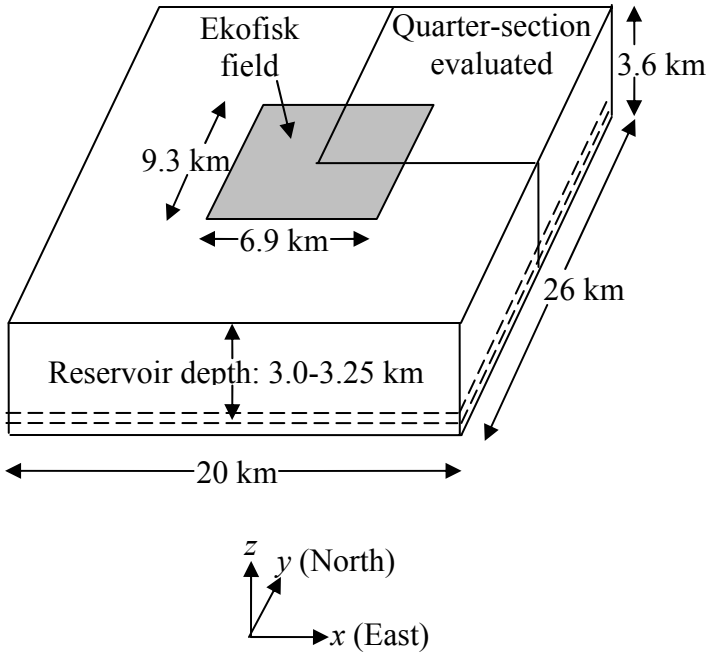

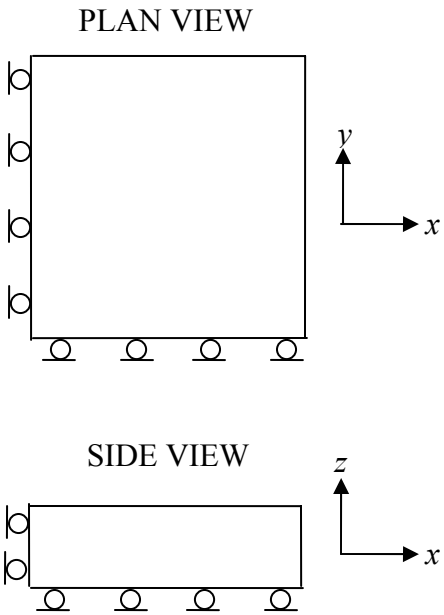

(a) **(b)**

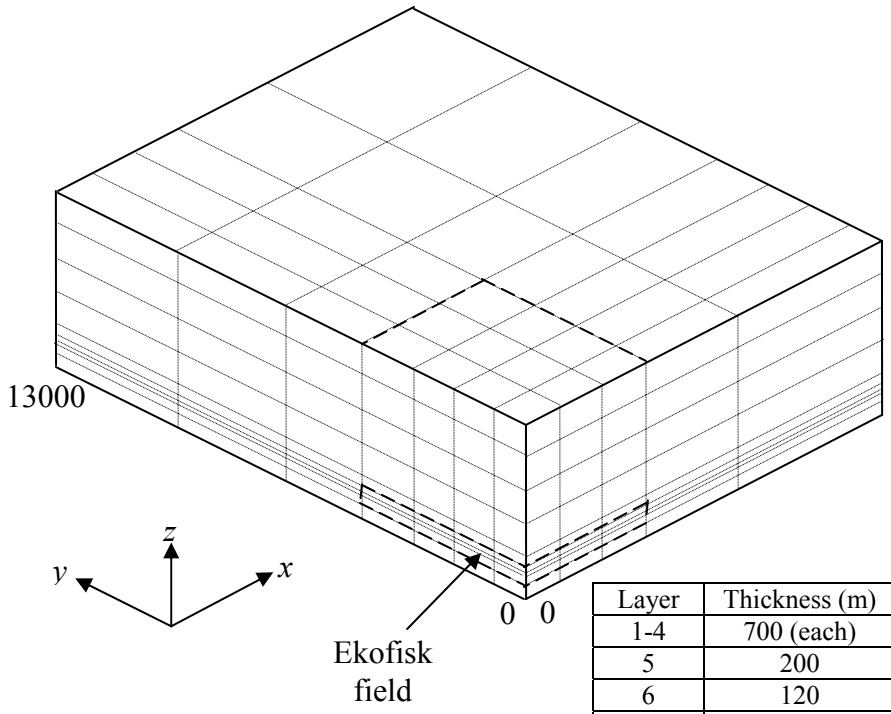

Layer	Thickness (m)	Material
1-4	700 (each)	Shale overburden
5	200	Shale overburden
6	120	Chalk (Ekofisk Fm.)
7	20	Chalk (tight zone)
8	110	Chalk (Tor Fm.)
9	350	Shale underburden

(c)

Figure 9.5. Geometry for field-scale simulations. (a) Dimensions of region evaluated; (b) finite element boundary conditions; (c) finite element mesh used.

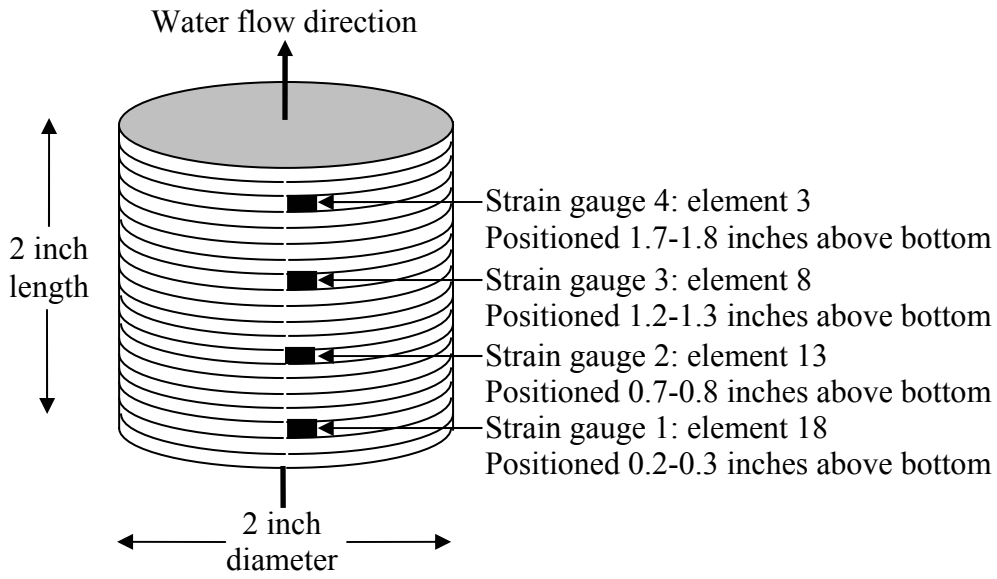

Figure 9.6. Positions of "strain gauges" for the laboratory-scale simulations. These are the local intervals over which strain is averaged and presented in Figures 9.7, 9.8, and 9.11. Results are also presented for average strain over the entire sample, which is equal to displacement of the top of the sample divided by the sample length.

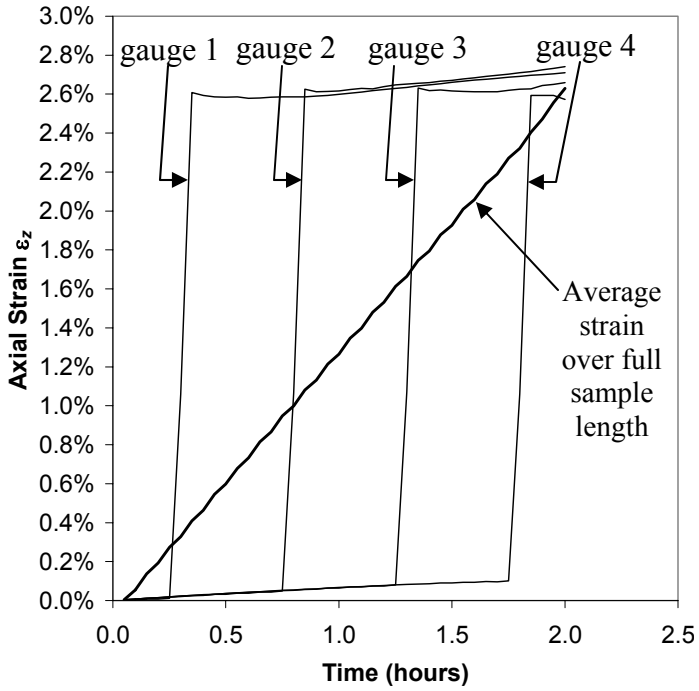

(a)

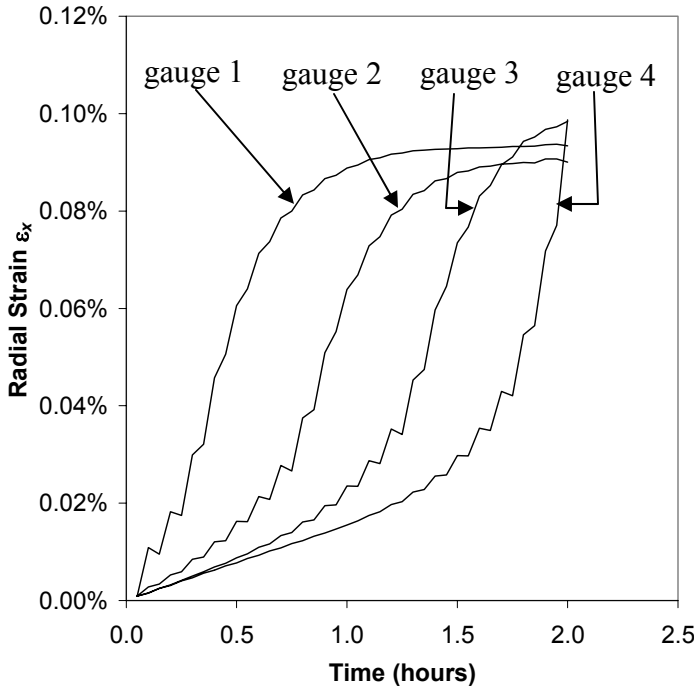

(b)

Figure 9.7. Strain histories at various localized intervals for a "fast" waterflooding test under near-K_0 stress conditions. For both (a) axial strains and (b) radial strains, strain occurs in a short time when the pore fluid changes from oil to water. Note that axial strains are much greater than radial strains for these stress conditions. Compare to Figure 9.8.

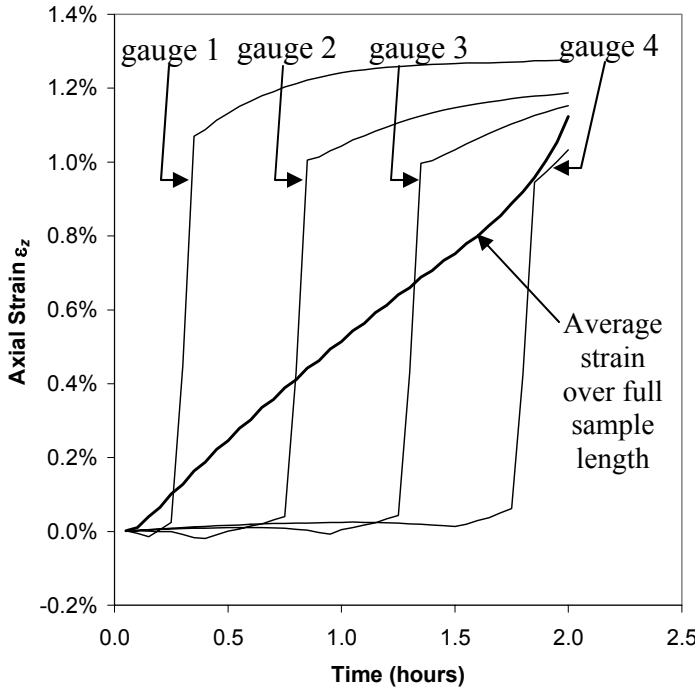

(a)

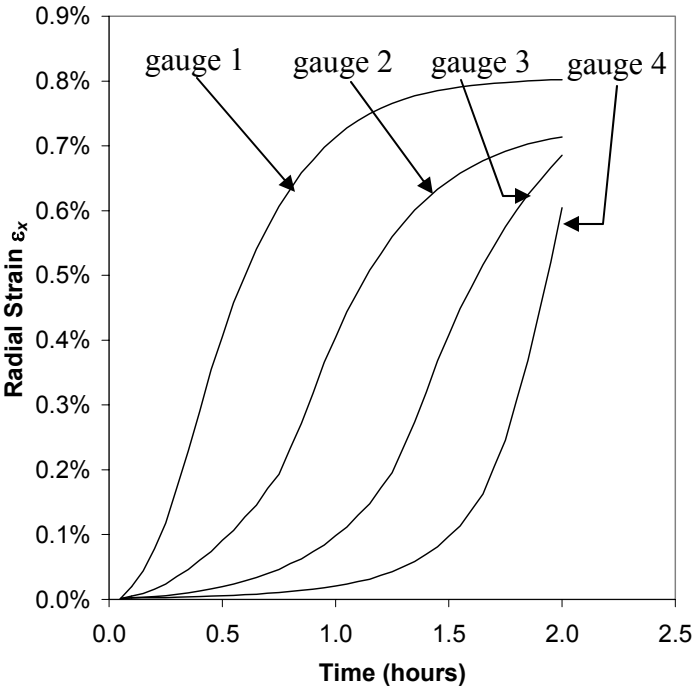

(b)

Figure 9.8. Strain histories at various localized intervals for a "fast" waterflooding test under hydrostatic stress conditions. For both (a) axial strains and (b) radial strains, strain occurs in a short time when the pore fluid changes from oil to water. Axial strains are only slightly greater than radial strains for these stress conditions. Compare to Figure 9.7.

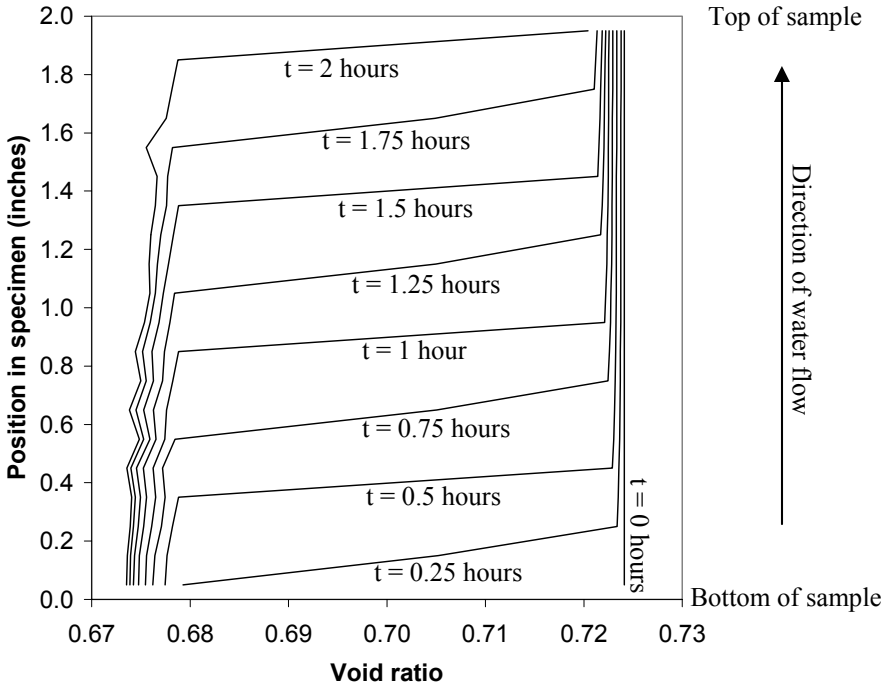

Figure 9.9. History of void space distribution during a "fast" waterflooding test under near-K_0 stress conditions. Void ratio in any interval decreases in a short time when the pore fluid changes from oil to water.

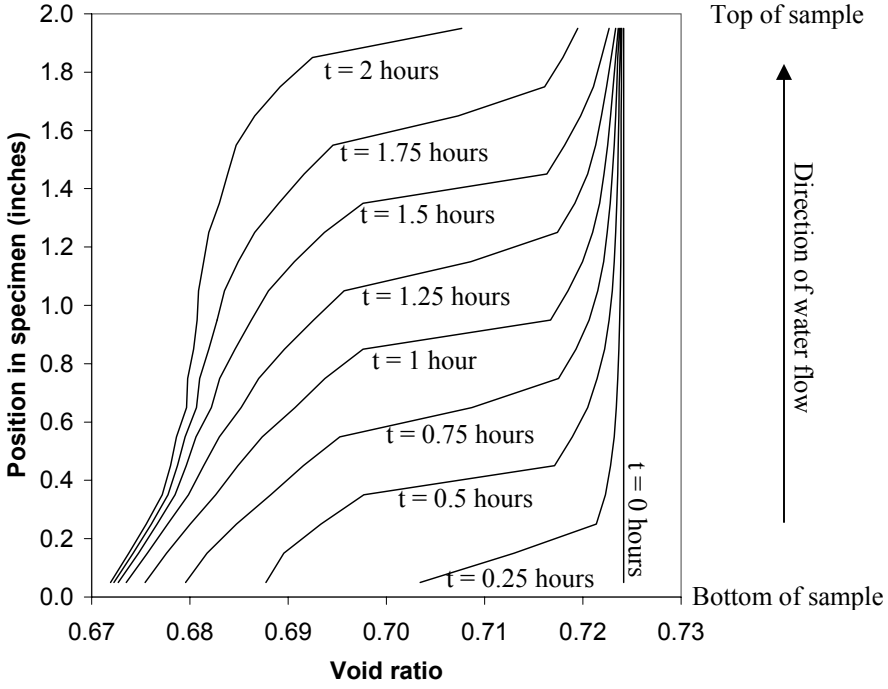

Figure 9.10. History of void space distribution during a "fast" waterflooding test under hydrostatic stress conditions. Void ratio in any interval decreases in a short time when the pore fluid changes from oil to water.

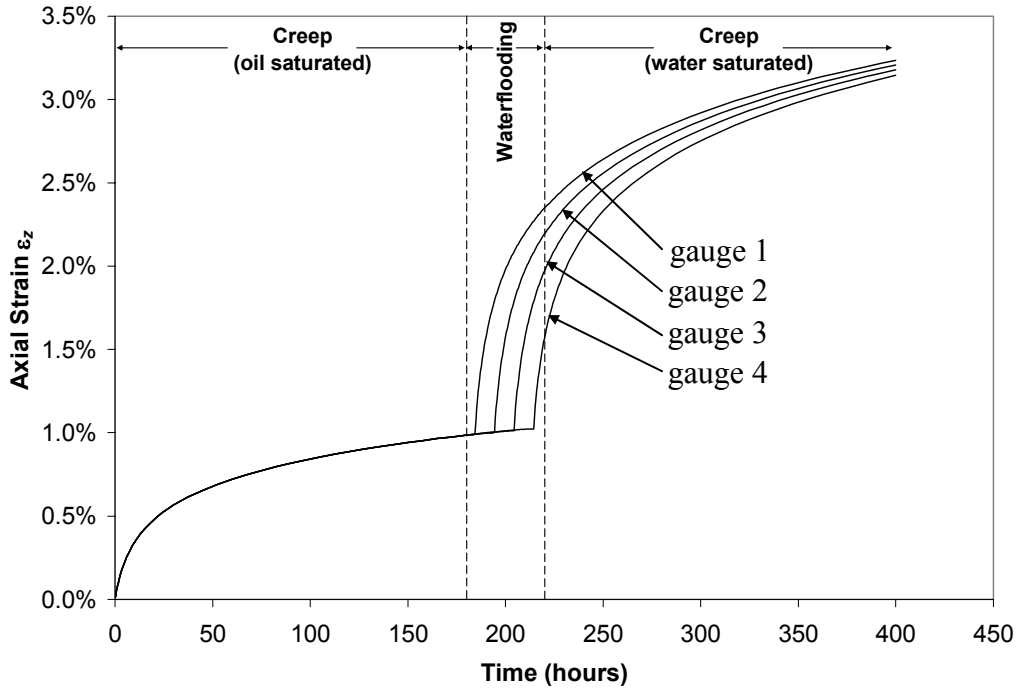

(a)

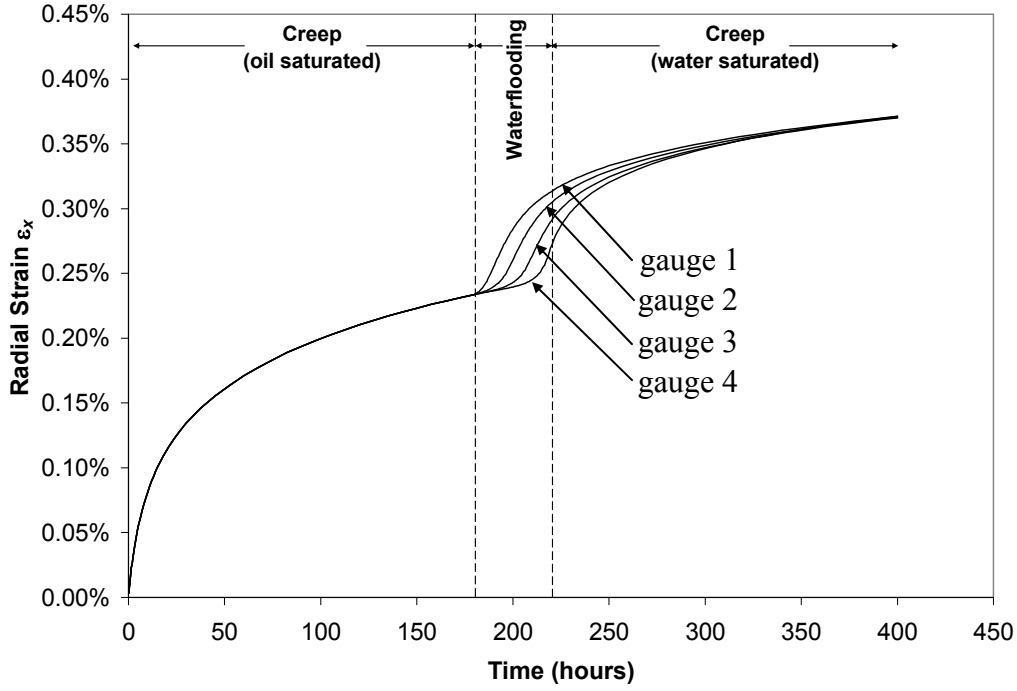

(b)

Figure 9.11. Strain histories at various localized intervals for a "slow" waterflooding test simulation under near-K_0 stress conditions, for a 20-element mesh. For both (a) axial strains and (b) radial strains, strain occurs in a short time when the pore fluid changes from oil to water. Axial strains are much greater than radial strains for near-K_0 conditions.

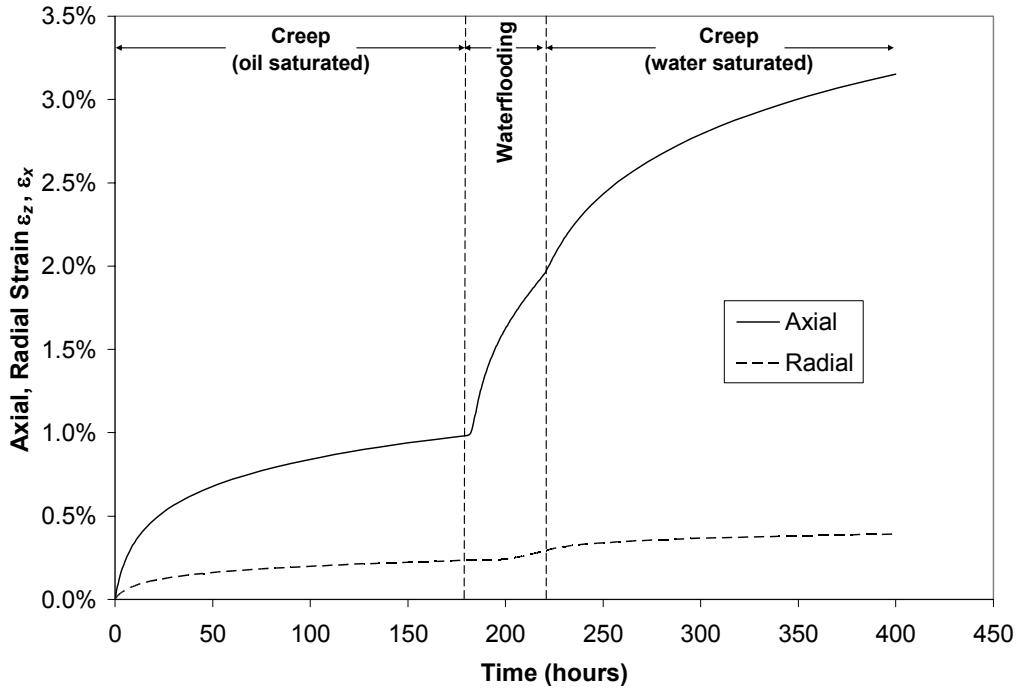

Figure 9.12. Strain histories for a "slow" waterflooding test simulation under near-K_0 stress conditions, for a 1-element mesh. Strain occurs in a short time when the pore fluid changes from oil to water. Axial strains are much greater than radial strains for near-K_0 conditions.

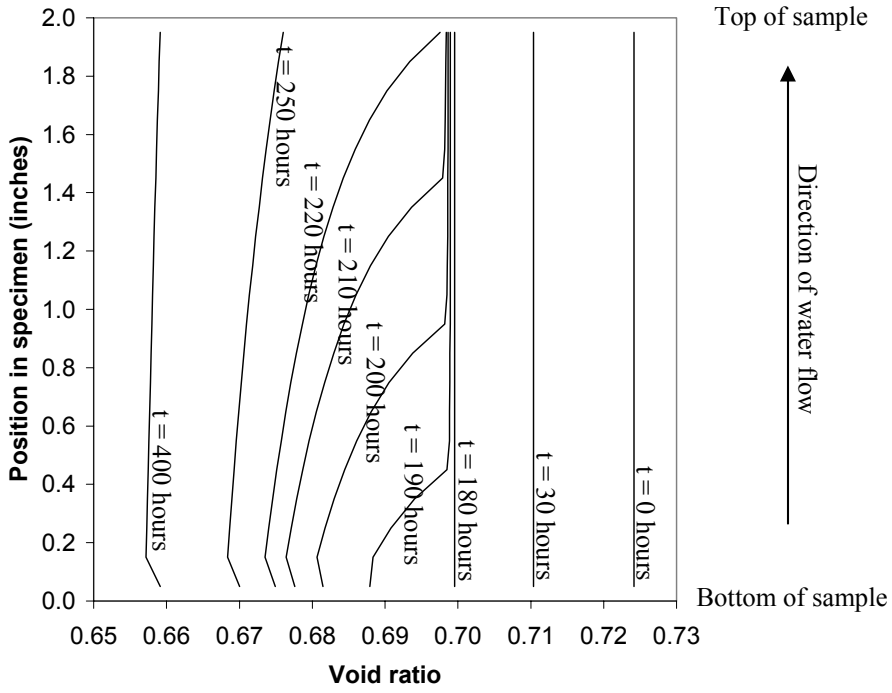

Figure 9.13. History of void space distribution during a "slow" waterflooding test simulation under near-K_0 stress conditions, for a 20-element mesh. More variability in void space distribution is seen than for "fast" waterflooding test; compare to Figure 9.9.

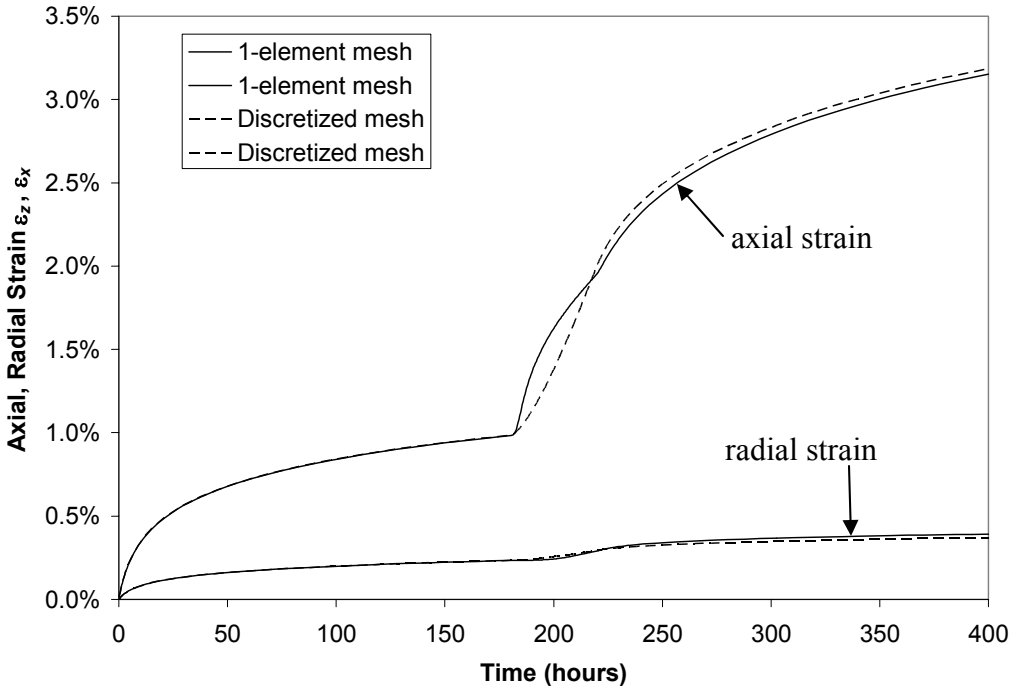

Figure 9.14. Comparison of average strain histories for a "slow" waterflooding test simulation under near-K_0 stress conditions, for a 1-element mesh and a 20-element mesh. The average strains in each sample are nearly identical, indicating that the procedure used to calculate average properties of chalk in an element with variability in pore fluid composition yields good results.

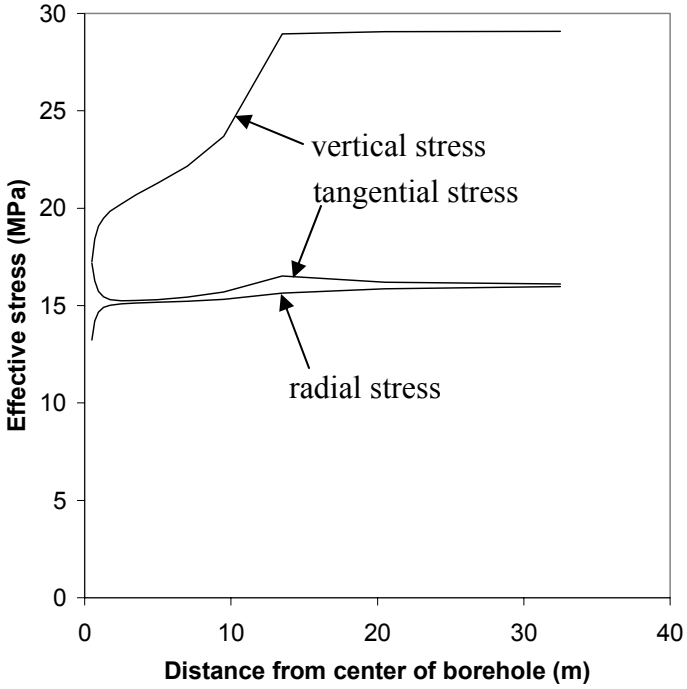

Figure 9.15. Stress distributions at the end of the simulation for the case in which waterflooding causes material weakening only.

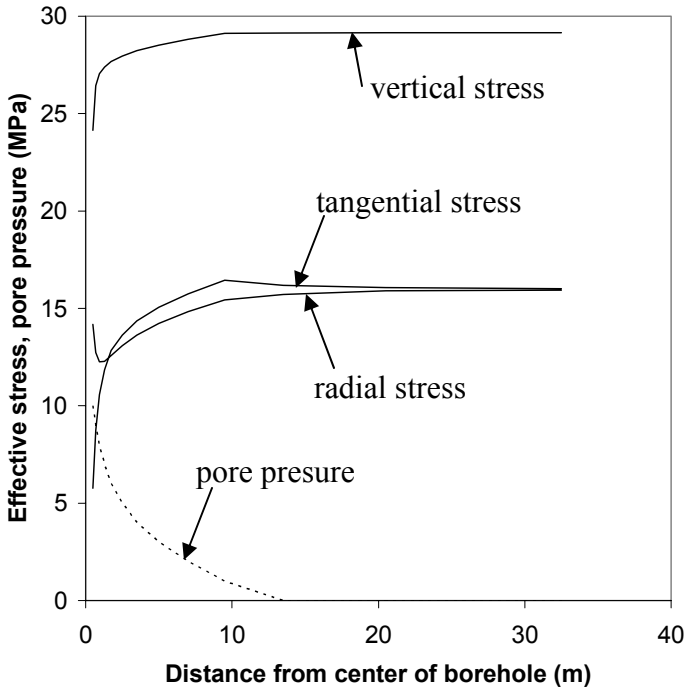

Figure 9.16. Stress distributions at the end of the simulation for the case in which waterflooding causes pore pressure increase only.

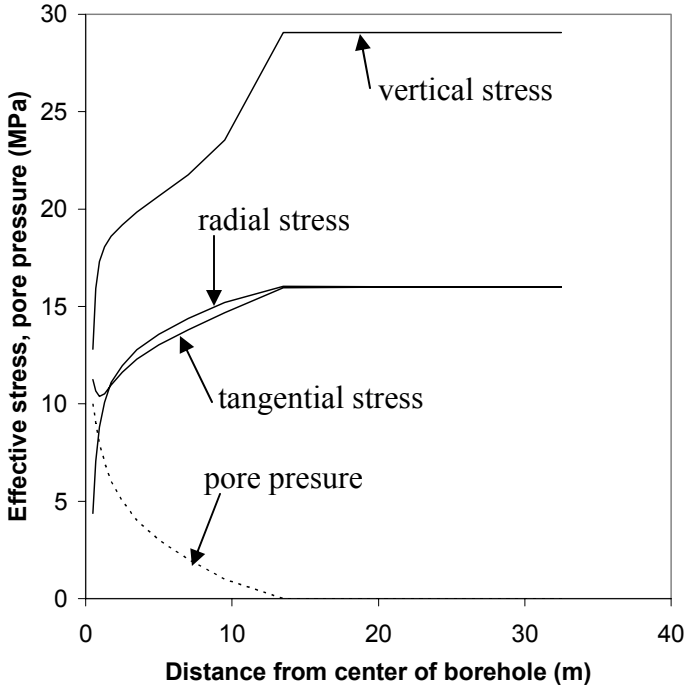

Figure 9.17. Stress distributions at the end of the simulation for the case in which waterflooding causes both pore pressure increase and material weakening.

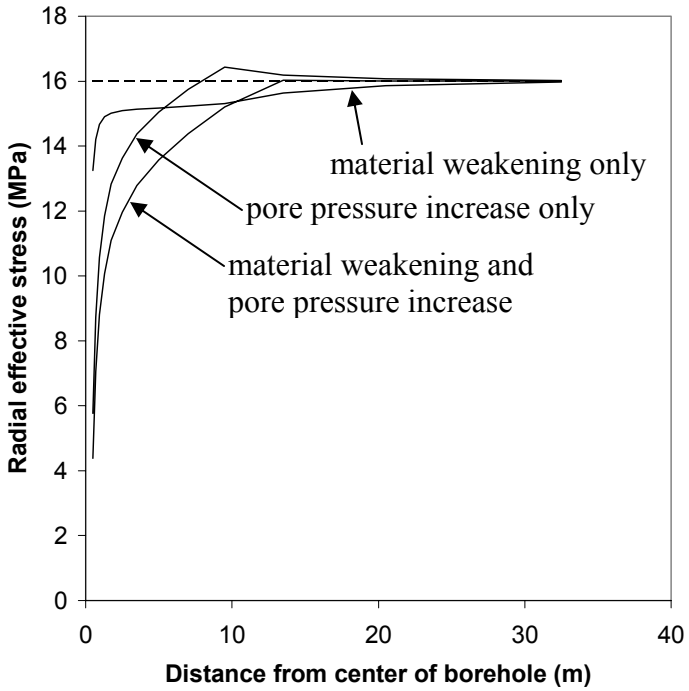

Figure 9.18. Comparison of radial stress distributions for three simulations in which waterflooding has different effects.

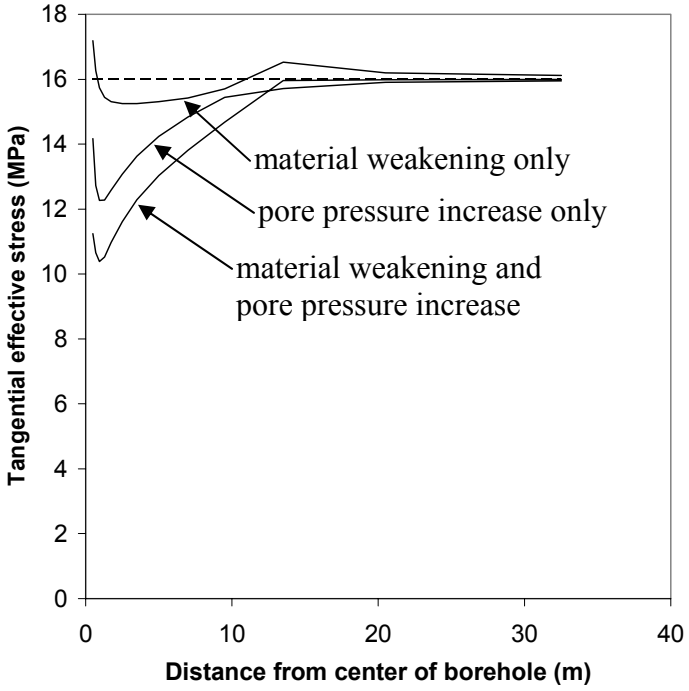

Figure 9.19. Comparison of tangential stress distributions for three simulations in which waterflooding has different effects.

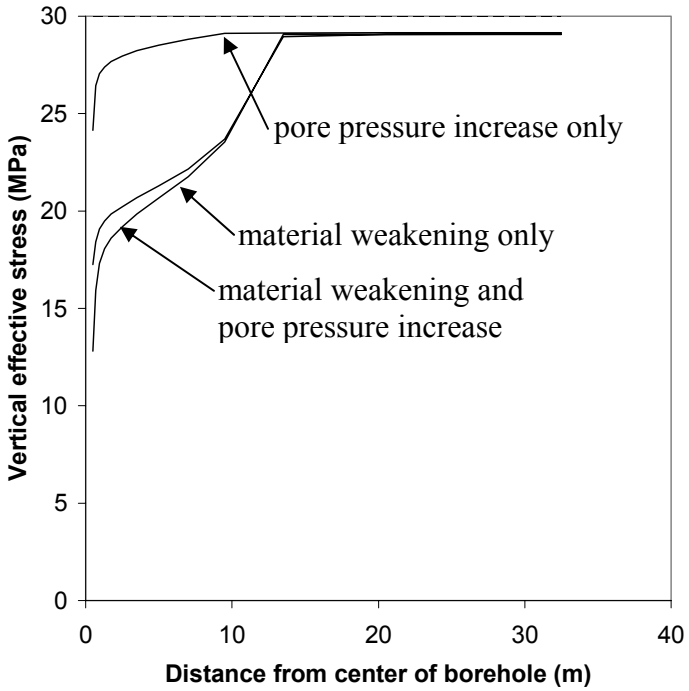

Figure 9.20. Comparison of vertical stress distributions for three simulations in which waterflooding has different effects.

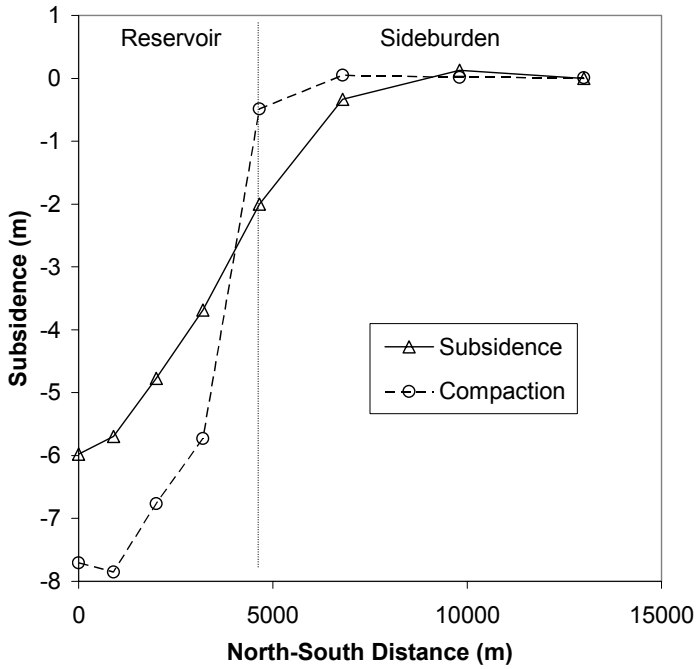

(a)

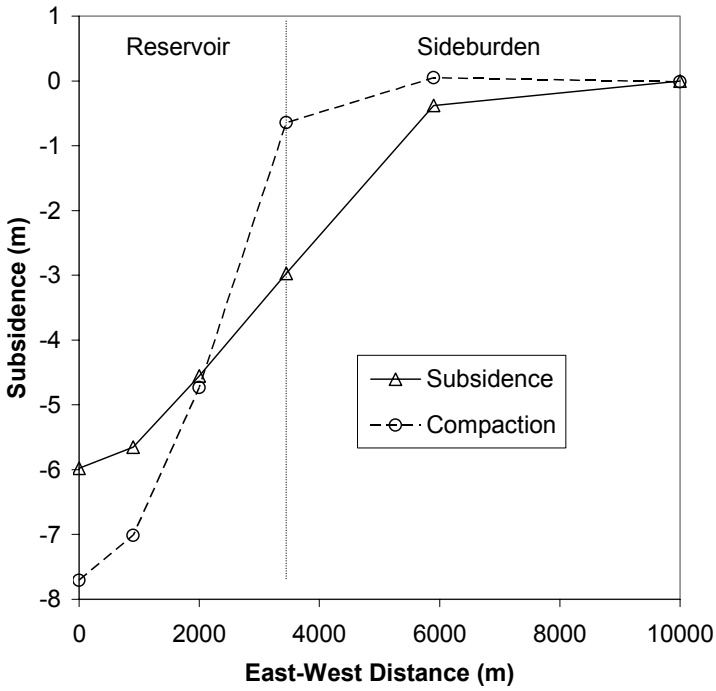

(b)

Figure 9.21. Compaction and subsidence profiles for the Ekofisk field for the case without water-weakening. Profiles are shown for (a) north-south direction; (b) east-west direction.

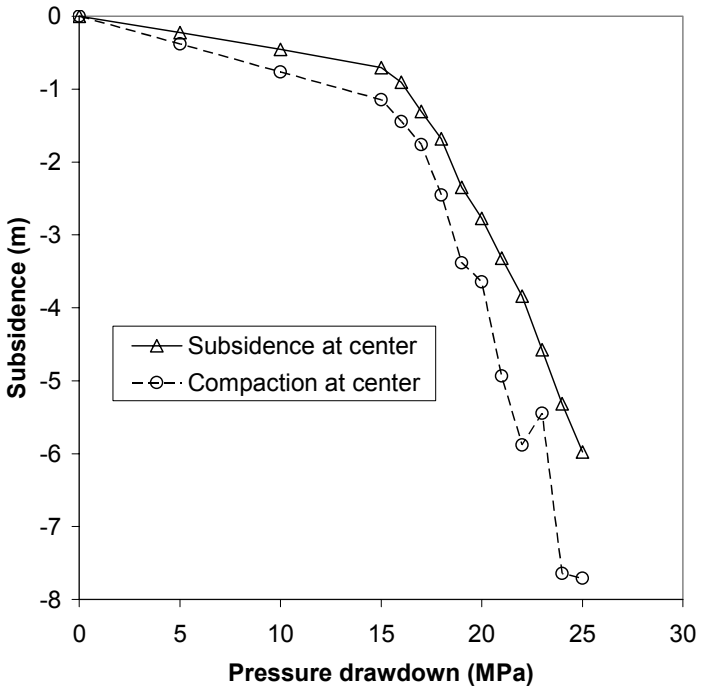

Figure 9.22. Compaction and subsidence history for the Ekofisk field for the case without water-weakening.

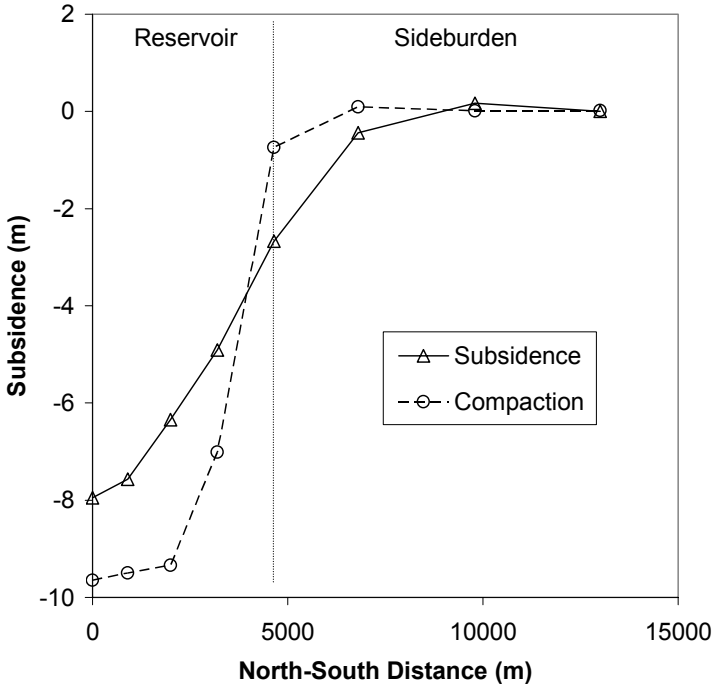

(a)

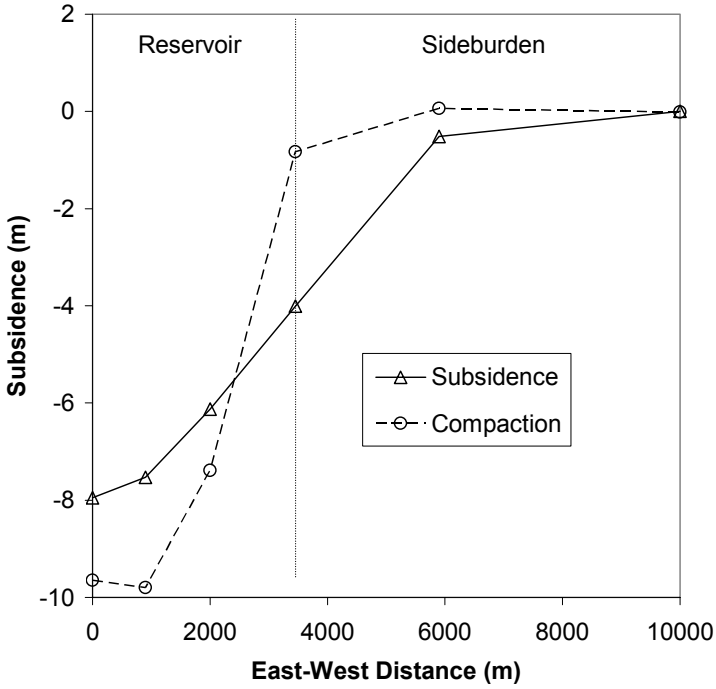

(b)

Figure 9.23. Compaction and subsidence profiles for the Ekofisk field for the case with water-weakening. Profiles are shown for (a) north-south direction; (b) east-west direction.

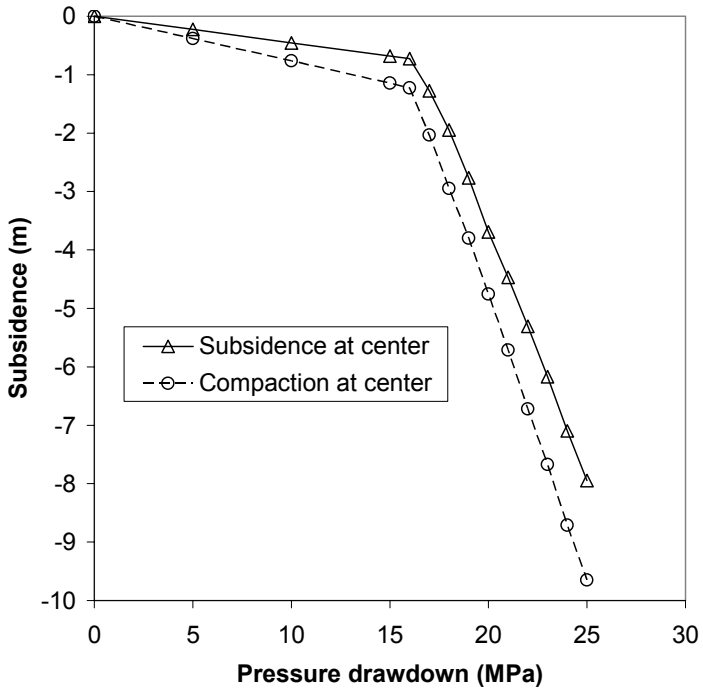

Figure 9.24. Compaction and subsidence history for the Ekofisk field for the case with water-weakening.